The 8th European Congress on Computational Methods in Applied Sciences and Engineering
ECCOMAS Congress 2022
5-–9 June 2022, Oslo, Norway

A POSTERIORI MOOD LIMITING APPROACH FOR MULTICOMPONENT FLOWS ON UNSTRUCTURED MESHES

P. Tsoutsanis[1], **P. S. Farmakis**[2,3,4]

[1] School of Aerospace, Transport and Manufacturing
Cranfield University,
Cranfield MK43 0AL, United Kingdom,
[2] Laboratory for Laser Energetics University of Rochester, NY, 14623, USA
[3] Flash Center for Computational Science, Department of Physics and Astronomy, University of Rochester, NY, 14627, USA
[4] Department of Mechanical Engineering, University of Rochester, NY, 14623, USA
email: panagiotis.tsoutsanis@cranfield.ac.uk, pfar@lle.rochester.edu

Key words: Multicomponent flows, Finite Volume, MOOD, CWENO

Abstract. A relaxed, high-order, Multidimensional Optimal Order Detection (MOOD) framework is extended to the simulation of compressible multicomponent flows on unstructured meshes in the open-source unstructured compressible flow solver `UCNS3D`. The class of diffuse interface methods (DIM) is employed with a five-equation model. The high-order CWENO spatial discretisation is selected due to its low computational cost and improved non-oscillatory behaviour compared to the original WENO variants. The relaxed MOOD enhancement of the CWENO method has been necessary to further improve the robustness of the CWENO method. A series of challenging compressible multicomponent flow problems have been implemented in `UCNS3D`, including shock wave interaction with a water droplet and shock-induced collapse of bubbles arrays. Such problems are generally very stiff due to the strong gradients present, and it has been possible to tackle them using the extended MOOD-CWENO numerical framework.

1 INTRODUCTION

Multi-component multi-phase compressible flows are encountered in several settings and their associated complicated interaction requires a good understanding of them in order to improve several processes and products that experience such flows. In this paper we employ the Eulerian framework and DIM. The DIM allows the treatment of a fluid interface which has a non-zero thickness. It is based on the idea originally formulated by Rayleigh (1892) [1] and van der Waals (1893) [2] who developed gradient theories for predicting the thickness of the interfaces based on thermodynamic principles. The mixing of the two states in the DI method is governed by the respective thermodynamic state of the two components involved. For mixing applications, one of the most common five-equation models is the one formulated by Allaire's et al. [3]. More complete models include the seven equation Baer-Nunziato's [4] framework that can additionally accommodate non-equilibrium effects, or the unified hyperbolic formulation of Godunov-Peshkov-Romenski (GPR model) [5, 6], and the reader is referred to the work of Maltsev et al. [7], for a comprehensive review of DIM.

In the present study, the five-equation model Allaire et al. [3] with an isobaric closure law is adopted, since it can simulate two fluids with arbitrary equations of state (EOS) for each of the fluid components. This simplified and compact five-equation model of Allaire et al. has found many applications, see for instance [8–17] and references therein. The hyperbolic character of the PDEs involved in this context; the simplicity of the particular type of DIM use; and their ease of implementation, are the main reasons for selecting the five-equation model of Allaire's et al. [3]. It should be noted at this point that DI methods can improve the resolution sharpness of the interfaces present in the computational domain and furthermore suppress any excessive diffusion across them when high-order, spatially high-resolution, oscillation-free numerical methods are used.

There are several very well established high-order high-resolution numerical methods in the unstructured finite-volume literature; however, in this study we will be focusing on the application of the Compact Weighted Essentially Non-Oscillatory (CWENO) type of schemes as developed in [18–20], since these methods were found to be more robust and significantly more computationally efficient compared to the original WENO-type of schemes for unstructured meshes, and their augmentation by the Multidimensional Optimal Order Detection (MOOD) algorithm. The augmented robustness provided by the MOOD technique is necessary for flow problems with very strong gradients that are common at interfaces between solids, liquids and gases under shock waves. All the schemes/models are developed in the open source community of the `UCNS3D` solver [21], and we assess their performance in terms of for a series of stringent 2-D and test problems.

The paper is organized as follows. In Section 2 we introduce the formulation of the governing equations employed for this study, followed by the numerical framework used to describe the high-order, finite-volume framework for unstructured meshes, the chosen fluxes and temporal discretisation used, and the MOOD algorithm in Section 3. In Section 4 the numerical results obtained for all the test problems are presented and compared against a relevant analytical, reference or experimental solution whenever possible. Finally, in the last section we put forward the conclusions drawn from this study.

2 GOVERNING EQUATIONS

The quasi-conservative five-equation model of Allaire [3] is used in this study and consists of two continuity equations eq. (1) and eq. (2), a momentum equation per dimension eq. (3), an energy equation eq. (4), and the non-conservative advection equation of the volume fraction of one of the two fluids eq. (5) as given below:

$$\frac{\partial(a_1\rho_1)}{\partial t} + \nabla \cdot (a_1\rho_1\mathbf{u}) = 0, \tag{1}$$

$$\frac{\partial(a_2\rho_2)}{\partial t} + \nabla \cdot (a_2\rho_2\mathbf{u}) = 0, \tag{2}$$

$$\frac{\partial\rho\mathbf{u}}{\partial t} + \nabla \cdot (\rho\mathbf{u}\mathbf{u} + p\mathbf{I}) = 0, \tag{3}$$

$$\frac{\partial E}{\partial t} + \nabla \cdot (E + p)\mathbf{u} = 0, \tag{4}$$

$$\frac{\partial a_1}{\partial t} + \mathbf{u} \cdot \nabla a_1 = 0, \tag{5}$$

where ρ is the density, $\mathbf{u} = (u, v, w)^T$ is the velocity, p is the pressure, E is the total energy and a is the volume fraction. The stiffened gas EOS is employed for closing the five-equation model with pressure for each state being given by:

$$p_i = (\gamma_i - 1)\rho_i \epsilon_i - \gamma_i \pi_{\infty,i}, \tag{6}$$

where $\pi_{\infty,i} \geq 0$ is a reference pressure, and will be set to $\pi_\infty = 0$ for gases. The total mass and $\rho\epsilon$ being given by:

$$\rho = \sum_i a_i \rho_i, \tag{7}$$

and $\rho\epsilon$ being

$$\rho\epsilon = \sum_i a_i \rho_i \epsilon_i, \tag{8}$$

where ϵ is the internal energy, with $\rho\epsilon \triangleq E - \frac{1}{2}\rho\mathbf{u}\mathbf{u}$. The EOS of the mixture reads

$$\xi \triangleq \frac{1}{\gamma - 1} = \sum_i \frac{a_i}{\gamma_i - 1}, \tag{9}$$

$$\frac{\pi_\infty \gamma}{\gamma - 1} = \sum_i a_i \frac{\pi_{\infty,i}\gamma_i}{\gamma_i - 1}, \tag{10}$$

$$p = (\gamma - 1)\rho\epsilon - \gamma\pi_\infty, \tag{11}$$

The non-conservative volume fraction advection Eq. (5) is rewritten in a mathematically equivalent form as introduced by Johnsen and Colonius [13]:

$$\frac{\partial a_1}{\partial t} + \nabla \cdot (a_1 \mathbf{u}) = a_1 \nabla \cdot \mathbf{u}. \tag{12}$$

3 NUMERICAL FRAMEWORK

3.1 Spatial Disretisation

Consider a 3-D domain Ω consisting of conforming tetrahedral, hexahedral, prism, and pyramid cells each one of them indexed by a unique mono-index i, and the governing equations of the five-equation model written in vector form as follows:

$$\frac{\partial}{\partial t}\int_{V_i} \mathbf{U}\, dV + \int_{\partial V_i} \mathbf{F}_n\, dS = \int_{V_i} \mathbf{s}\, dV, \tag{13}$$

where $\mathbf{U} = \mathbf{U}(\mathbf{x}, t)$ is the vector of conserved variables and the volume fraction of one species, $\mathbf{F}_n$ is the non-linear flux in the direction normal to the cells interface as given below:

$$\mathbf{U} = \begin{bmatrix} a_1\rho_1 \\ a_2\rho_2 \\ \rho u \\ \rho v \\ \rho w \\ E \\ a_1 \end{bmatrix}, \mathbf{F}_n = \begin{bmatrix} a_1\rho_1 u_n \\ a_2\rho_2 u_n \\ \rho u u_n + n_x p \\ \rho v u_n + n_y p \\ \rho w u_n + n_z p \\ u_n(E+p) \\ a_1 u_n \end{bmatrix}, \tag{14}$$

where u_n is the velocity normal to the bounded surface area, defined by $u_n = n_x u + n_y v + n_z w$. The source term $\mathbf{s}$ is with regards to the term $a_1 \nabla \cdot \mathbf{u}$ of Eq. (5). Following the approach of Johnsen and Colonius [13] the source term is numerically approximated as surface integral, rather than a volume one, while using the same velocity estimate as the one used for the evaluation of the fluxes as shown below:

$$\int_{V_i} a_1 \nabla \cdot \mathbf{u} \, dV \approx \int_{V_i} a_1 \, dV \cdot \int_{\partial V_i} (u_n)^{Riem.} \, dS. \tag{15}$$

Integrating Eq. (13) over the mesh element i using a high-order explicit finite-volume formulation the following equation is obtained that incorporates the source term as previously defined:

$$\frac{d\mathbf{U}_i}{dt} = \frac{1}{|V_i|} \sum_{j=1}^{N_f} \sum_{\alpha=1}^{N_{qp}} \left(F_{\mathbf{n_{ij}}} \left(\mathbf{U}^n_{ij,L}(\mathbf{x}_{ij,\alpha}, t), \mathbf{U}^n_{ij,R}(\mathbf{x}_{ij,\alpha}, t) \right) - \mathbf{a}^n_{i,1} \cdot u_n^{Riem}(\mathbf{x}_{ij,\alpha}, t) \right) \omega_\alpha |S_{ij}|, \tag{16}$$

where $\mathbf{U}_i$ is the volume averaged vector of variables

$$\mathbf{U}_i = \frac{1}{|V_i|} \int_{V_i} \mathbf{U}(x, y, z) \, dV, \tag{17}$$

and $F_{\mathbf{n_{ij}}}$ is a numerical flux function in the direction normal to the cell interface between a considered cell i and one of its neighbouring cells j. N_f is the number of faces per element, N_{qp} is the number of quadrature points used for approximating the surface integrals, $|S_{ij}|$ is the surface area of the corresponding face, and $\mathbf{U}^n_{ij,L}(\mathbf{x}_{ij,\alpha}, t)$ and $\mathbf{U}^n_{ij,R}(\mathbf{x}_{ij,\alpha}, t)$ are the high-order approximations of the solutions for cell i and cell j respectively. α corresponds to different Gaussian integration points $\mathbf{x}_\alpha$ and weights ω_α over each face. $\mathbf{a}^n_{i,1}$ corresponds to the volume averaged volume fraction of cell i at time level n. The volume, surface and line integrals are numerically approximated by a suitable Gauss-Legendre quadrature.

The reconstruction process adopted in `UCNS3D` [21, 22] follows the approaches of Tsoutsanis et al. [19, 20, 23, 24], Titarev et al. [25] that have been previously applied to smooth and discontinuous flow problems [19–21, 23–43] and the reader is referred to previous work [19] which documents the particular CWENO variant used in this study.

3.2 Fluxes approximation & Temporal discretisation

For the inviscid fluxes the approximate HLLC (Harten-Lax-van Leer-Contact) Riemann solver of Toro [44] is employed, unless otherwise stated. The temporal discretisation employs the 3^{rd}-order explicit Strong Stability Preserving (SSP) Runge-Kutta method [45] which is stable for $CFL \leq 1$ and a $CFL = 0.6$ is used for all test-problems unless otherwise specified. All the volume/surface/line integrals are approximated by Gaussian quadrature rule suitable for the order of polynomial employed. It has to be noted that the reconstruction in the present study is carried out with respect to the primitive variables by transforming to them only during the reconstruction process, while always transforming to conservative variables prior to the fluxes calculation. All the schemes developed are implemented in the open-source `UCNS3D` [21] CFD code using object-oriented Fortran 2003, and employing MPI message passing interface (MPI), and the Open Multi-Processing (OpenMP) application programming interface (API). The reader is referred to [35, 46] for more details on implementation and performance benchmarks.

3.3 MOOD

The relaxed MOOD algorithm [36] is a unique *a posteriori* method to enhance the non-oscillatory properties of any numerical method. In this study relaxed version developed by Farmakis et al. [36] is employed which has been previously tested successfully for very intensive computational problems with sharp discontinuities, density and velocity gradients, f.e. high-speed 2-D and 3-D converging flows perturbed by the Rayleigh-Taylor and Richtmyer-Meshkov instabilities. The main goal is to extend it to multicomponent flow problems. The key ingredient of the MOOD algorithm is that for all the cells in the computational domain, a candidate solution should be both physically and numerically admissible. If these conditions are not satisfied in a given cell, the order of accuracy of the scheme is reduced locally until the candidate solution is admissible. Specifically, following the solution of the fluxes, each candidate solution calculated using any of the high-order methods implemented in `UCNS3D` (such as Central, CWENO, MUSCL, etc.) will be passed through two detectors:

1. *Physical Admissible Detector* (PAD): This detector checks that the solution is physical, that is, all points must have positive density and positive pressure at all times. In essence, this detector will identify any point exhibiting NaN values.

2. *Numerical Admissible Detector* (NAD): This is a more flexible version of the Discrete Maximum Principle (DMP). The detector checks that the solution is monotonic, and that no new extrema are created. It compares the candidate solution with the solution obtained in the previous Runge-Kutta step.

If the candidate solution does not satisfy the PAD & NAD criteria, the code falls back to an *auxiliary* 2nd-order MUSCL scheme, and a relaxed version of the PAD & NAD criteria are applied again. This transition with more relaxed criteria has been carefully selected to maintain the solution of a cell both admissible and of the highest possible order. In case the new candidate solution is also not admissible, then the code *parachutes* to the *bulletproof* scheme. For `UCNS3D`, this is Godunov's flux. Being a first-order Upwind scheme, Godunov's method is known to satisfy the PAD & NAD criteria by definition. At this point, it should be noted that

MOOD's *a posteriori* nature gives rise to one important complication that the solutions for its neighbouring cells will have to be recomputed as well; these solutions might be contaminated by the stricken cell's solution through the flux operation.

The entire operation of the MOOD implementation of Farmakis et al. in `UCNS3D` can be seen in the flow chart in Fig. 1. The collection of cells $\mathcal{V}_i$ represents the set of first neighbours of the cell i in consideration. In its present form, the NAD criterion assesses the conservative variables' vector, as suggested by [47]. The candidate solution $\mathbf{U}_i^*$for a cell i during any Runge-Kutta stage should be within a certain range provided by the $\mathcal{V}_i$ region defined previously. The superscript $(^n)$ indicates here the previous Runge-Kutta step, not the previous time step:

$$\min_{y\in\mathcal{V}_i}(\mathbf{U}^n(y)) - \delta \leq \mathbf{U}_i^* \leq \min_{y\in\mathcal{V}_i}(\mathbf{U}^n(y)) + \delta\,. \tag{18}$$

The original DMP-relaxed margins can be seen in step 6a. of the flow chart. Denoted by $(^\circ)$, they read:

$$\delta^\circ = \max_{y\in\mathcal{V}_i}\left(10^{-4}, 10^{-3}\cdot\left[\max_{y\in\mathcal{V}_i}(\mathbf{U}^n(y)) - \min_{y\in\mathcal{V}_i}(\mathbf{U}^n(y))\right]\right), \tag{19}$$

while the "tempered" criteria, employed in step 6b. of the flow chart and denoted by $\left(^R\right)$, ensure a prudent, as well as smooth transition along the cascade, from second to first order of accuracy. They are selected as:

$$\delta^R = \max_{y\in\mathcal{V}_i}\left(10^{-4}, 10^{-1}\cdot\left[\max_{y\in\mathcal{V}_i}(\mathbf{U}^n(y)) - \min_{y\in\mathcal{V}_i}(\mathbf{U}^n(y))\right]\right). \tag{20}$$

The relaxed criteria, developed for the `UCNS3D`, reduce significantly the computational overhead of the MOOD method, without reducing the efficacy of the framework to ensure the non-oscillatory properties solution. This has to do also with the favourable non-oscillatory properties of the limiters employed for the 2nd-order MUSCL scheme as reported by Tsoutsanis [37].

It has to be stressed that for the present MOOD implementation all the flow variables are subject to the NAD criteria including the volume fraction. For more details regarding the implementation and testing of the algorithm, the readers are referred to the work of Farmakis et al. [36].

4 RESULTS AND DISCUSSION

4.1 Multicomponent convergence test

For assessing the impact of the MOOD technique for smooth flow problems and the designed order of spatial accuracy of the selected numerical method, a multicomponent advection test introducted by Wong and Lele [12] is used. In this test, a smooth volume fraction initial profile of two gases is advected for one period in a periodic computational domain. The initial condition

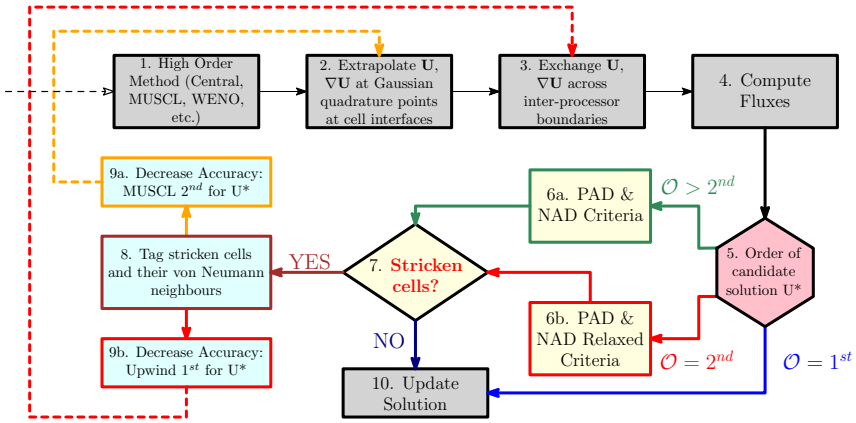

Figure 1: Flow-chart of the MOOD-augmented `UCNS3D` code. In its current configuration, the high-order numerical scheme selected by the user (Central, CWENOZ, MUSCL, etc.) passes on the information of the fluxes to the *a posteriori* MOOD algorithm. The switch between accuracy criteria for the PAD/NAD sensors is shown as steps 5, 6a, and 6b. Step 9a is the transition from a higher order to the first *auxiliary* (2^{nd} order MUSCL), while 9b is *parachuting* the solution to the *bulletproof*, first order accurate Godunov's flux. A solution decremented to first order is exempted of the PAD/NAD due to its conservativity property.

is given by:

$$(\rho_1, \rho_2, u, v, p, a_1) = (7, 1, 1, 0, 1/1.4, 0.5 + 0.25\sin(2\pi(x - 0.5))) \,. \tag{21}$$

The 2-D computational domain $[0, 1]^2$ consists of arbitrary unstructured triangular elements of 10, 20, 40 and 80 edges per side resolution, and the simulation is run for a time of $t_f = 1$. The two gases selected for this test are nitrogen and helium with specific heats 1.4 and 1.66 respectively. The numerical errors e_{L^2} and the e_{L^∞} are computed as follows:

$$e_{L^2} = \sqrt{\frac{\sum_i \int_{\Omega_i} \left(\mathbf{U}_e\left(x, t_f\right) - \mathbf{U}_c\left(x, t_f\right)\right)^2 dV}{\sum_i |\Omega_i|}}, \tag{22}$$

$$e_{L^\infty} = \mathcal{M}ax \left|\left(\mathbf{U}_e\left(x, t_f\right) - \mathbf{U}_c\left(x, t_f\right)\right|\right., \tag{23}$$

where $\mathbf{U}_c\left(x, t_f\right)$ and $\mathbf{U}_e\left(x, t_f\right)$ are the computed and exact solutions at the end of the simulation $t_f = 1.0$ (normalized time). The exact solution $\mathbf{U}_e\left(x, t_f\right)$ is given by the initial condition itself at $t = 0$. The simulations were performed with a $CFL = 0.1$ to ensure a sufficiently small time-step size. This made it possible to achieve the designed order of spatial accuracy. The wallclock time per simulation is normalised with respect to the fastest time recorded for this class of test problems; this was given by the CWENO3 scheme on the coarsest mesh.

Inspecting the calculated orders of convergence for all the schemes used in this particular problem in Table 1, makes it clear that the present MOOD variant provides the same order of accuracy as the embedded numerical method, with a small computational overhead (3-12%) due to the PAD/NAD condition checking.

Table 1: e_{L^∞} and e_{L^2} errors, and convergence orders of the schemes with respect to volume fraction and normalised wallclock time for the 2-D multi-species convergence test at normalized $t = 1.0$. It can be noticed that the MOOD-CWENO variant achieve the same order of accuracy as the CWENO variant, with a small computational overhead (3-12%) due to the PAD/NAD condition checking.

	CWENO					MOOD-CWENO				
Order/Edges per side	e_{L^∞}	O_{L^∞}	e_{L^2}	O_{L^∞}	$Time$	e_{L^∞}	O_{L^∞}	e_{L^2}	O_{L^∞}	$Time$
$3rd/10$	1.124E-02	-	6.897E-03	-	1.000	1.124E-02	-	6.897E-03	-	1.03
$3rd/20$	1.514E-03	2.89	9.535E-04	2.85	8.240	1.514E-03	2.89	9.535E-04	2.85	8.35
$3rd/40$	1.993E-04	2.93	1.244E-04	2.94	85.831	1.993E-04	2.93	1.244E-04	2.94	93.67
$3rd/80$	2.487E-05	3.00	1.581E-05	2.98	673.159	2.487E-05	3.00	1.581E-05	2.98	690.56
$4th/10$	1.879E-03	-	5.355E-04	-	1.530	1.879E-03	-	5.355E-04	-	1.59
$4th/20$	7.487E-05	4.65	2.762E-05	4.28	10.864	7.487E-05	4.65	2.762E-05	4.28	12.32
$4th/40$	4.962E-06	3.92	1.857E-06	3.89	115.068	4.962E-06	3.92	1.857E-06	3.89	126.78
$4th/80$	3.482E-07	3.83	1.200E-07	3.95	928.223	3.482E-07	3.83	1.200E-07	3.95	944.92
$5th/10$	9.115E-04	-	4.777E-04	-	1.650	9.115E-04	-	4.777E-04	-	1.79
$5th/20$	2.994E-05	4.93	1.736E-05	4.78	13.055	2.994E-05	4.93	1.736E-05	4.78	14.27
$5th/40$	1.084E-06	4.79	5.816E-07	4.90	139.432	1.084E-06	4.79	5.816E-07	4.90	148.31
$5th/80$	3.327E-08	5.03	1.883E-08	4.95	1119.209	3.327E-08	5.03	1.883E-08	4.95	1251.92

4.2 Water column in air

The second class of numerical tests involves a shock wave interacting with a cylindrical water column, following a test case of Xiang and Wang [48]. A water droplet is surrounded by air, where a shockwave at $M_{sh} = 2.4$ is moving towards the water bubble. This is an ideal test problem for assessing the limits of the MOOD algorithm in terms of its robustness. In our study, we consider a variant of the original test, and we remove the air cavity in the water column. This way we can directly compare the computational results with available experiments. We show the setup of the test problem in this work on the right of Fig. 2 for which $r = 0$, alongside the original test problem on the left where the water column has an air cavity $r = 3.6mm$.

The initial condition is given by:

$$(\rho, u, v, p, \gamma, \pi_\infty, a_1) = \begin{cases} \left(3.85, 567.3, 0, 0.664 \cdot 10^6, 1.4, 0, 0\right), & \text{for Post-shock} \\ \left(1.2, 0, 0, 0.101 \cdot 10^6, 1.4, 0, 0\right), & \text{for Pre-shock} \\ \left(1000, 0, 0, 10^5, 6.12, 0.343 \cdot 10^9, 1\right), & \text{for Water} \end{cases} \tag{24}$$

The domain is $x \in [0, 0.2208], y \in [0, 0.1152]$; the water column is centred at $(0.0576m, 0.0576m)$, and the interface between shocked and unshocked regions is located at $x = 0.05m$. Non-reflecting boundary conditions are used at the left and right boundaries of the domain, and a slip-wall is applied for the top and bottom boundaries. A quadrilateral mesh with approximately 0.89 million cells and an average edge length of $e_c \approx D_b/192$, where D_b is the diameter of the water column. The CWENO3-MOOD scheme was employed for this test problem, and the simulation is run until the non-dimensional $t^* = tu/D_b = 10$ where u corresponds to the initial velocity be-

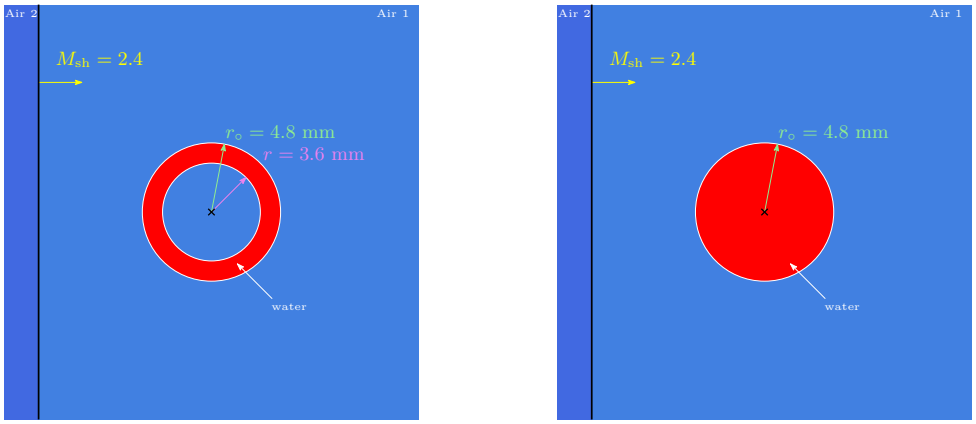

Original test case. Present work.

Figure 2: Schematic diagram of the original setup (left figure) and the present work (right figure) for the shock wave cylindrical water column test problem.

hind the shock. All the key flow features, including the reflected expansion wave, the transmitted wave, and the Mach stem are correctly captured as shown in comparison with the experimental results for the water column without cavity of Sembian et al. [49] in Fig. 3.

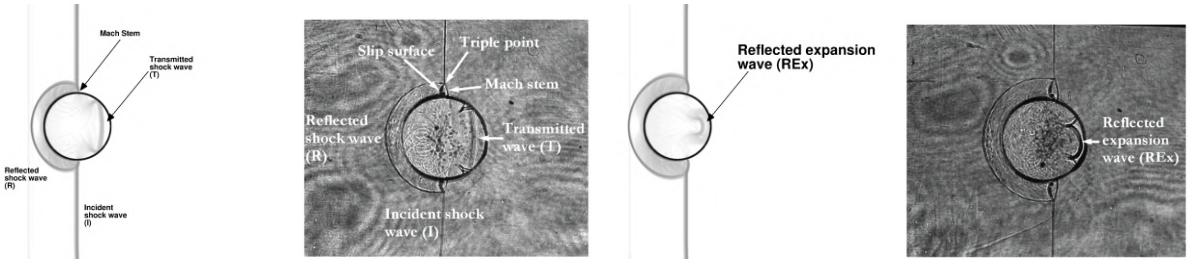

Figure 3: Numerical Schlieren contours computed in this work (top) and obtained by experiments of Sembian et al. [49] (bottom) for the shock-wave interaction with a water column at $M = 2.4$.

The computed density gradient magnitude is in good agreement with the numerical results of Xiang and Wang [48] as shown in Fig. 4, and it can be noticed that the MOOD algorithm has switched some regions to the first-order bulletproof scheme due to the stiff gradients encountered in those flow regions. At late times the flow separates, as seen in Fig. 4; the water column is compressed continuously while it gets flattened downstream, in agreement with what is documented by Xiang and Wang [48], and Meng and Colonius [50].

4.3 Shock-induced collapse of bubble arrays

As a third numerical study, we consider the collapse of an array of bubbles triggered by an advancing shockwave. In particular, we are using the bubble array setup introduced by Bempedelis and Ventikos [51]. The goal of this investigation is to understand the performance of the developed MOOD-CWENO algorithm in this test problem, where a high-energy concentration

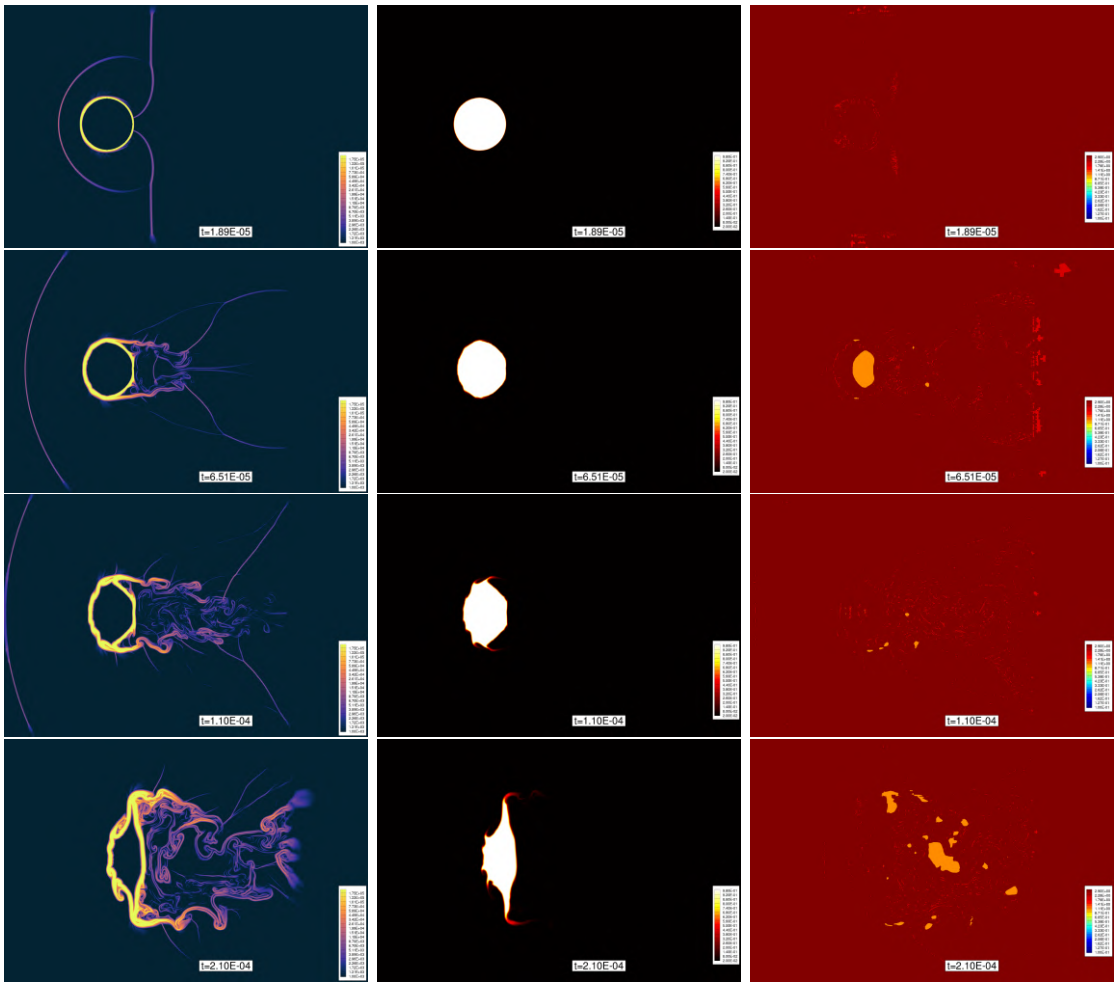

Figure 4: Contour plots of density gradient magnitude (left), volume fraction(middle) and mood enabled regions (right) of the computed solution of the shock wave interaction with a water column with, at various instants (left to right).

occurs during the shock-induced collapse of a bubble array. We are considering a 2-D arrangement of an array of three bubbles arranged in a triangular shape as shown in Fig. 5. The radius of the small bubble is $R_b = 0.0002m$ and the radius of the large bubbles is set to $R_B = 0.0005m$. The radius of the small bubble is $R_b = 0.0002m$ and the radius of the large bubbles is set to $R_B = 0.0005m$. Post-shock conditions correspond to a Mach number of $M = 1.72$, and the initial condition for both gases are given by:

$$(\rho, u, v, p, \gamma, \pi_\infty, a_1) = \begin{cases} (1, 0, 0, 100000, 1.4, 0, 0)\,, & \text{for gas bubbles} \\ \left(1323, 0, 0, 100000, 4.4, 6 \cdot 10^8, 1\right), & \text{for Water} \end{cases} \tag{25}$$

The domain is discretised by three quadrilateral meshes of resolution equivalent to 200, 100, and 50 points per large bubble radius respectively. The simulation is run for $t = 1.2\mu s$. For this

problem a CWENO5-MOOD method is employed, fortifying the robustness of the CWENO5 method for this challenging test problem.

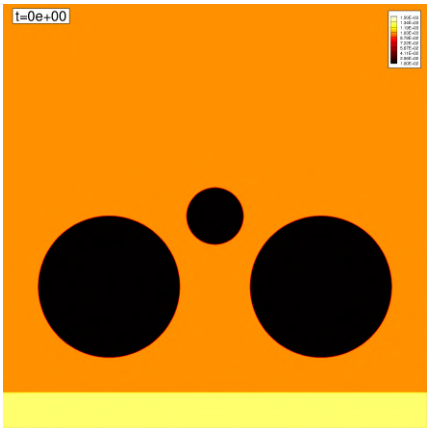

Figure 5: Schematic diagram showing the setup for the triangular bubble array test problem

From the obtained results at different times, shown in Fig. 6, Fig. 7, and Fig. 8, our results agree follow the same trends as the results of Bempedelis and Ventikos [51], both in terms of flow-structures as well as the expected pressure peak during the simulation. The pressure histories from our simulations are shown in Fig. 9, where different grid resolutions are used.

It needs to be stressed that without the MOOD extension, simulating this flow problem with a high-order scheme like the CWENO5 would not be feasible. This is because of the stiffness in those regions where a lot of energy is concentrated. Those regions can be seen in Fig. 8. Several cells marked belong to these regions, and for these cells, the solver resorted to 2nd-order MUSCL or even 1st-order method to ensure that the PAD and NAD criteria are satisfied. Without the MOOD algorithm keeping monotonicity violations in check, it is clear that the originally minute oscillations in the solution would avalanche, crashing the simulation.

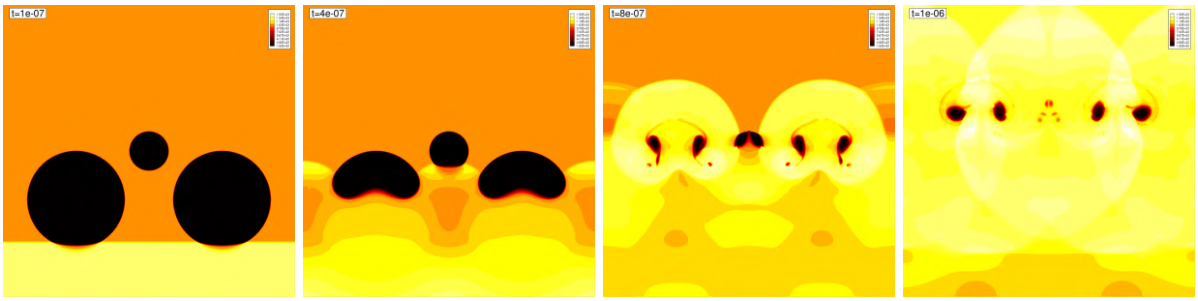

Figure 6: Contour plots of density for the bubble array shock-induced collapse test problem at different times.

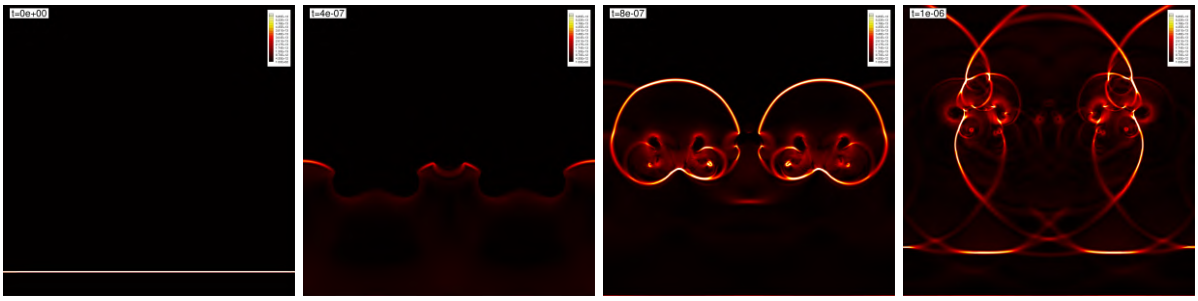

Figure 7: Contour plots of pressure for the bubble array shock-induced collapse test problem at different times.

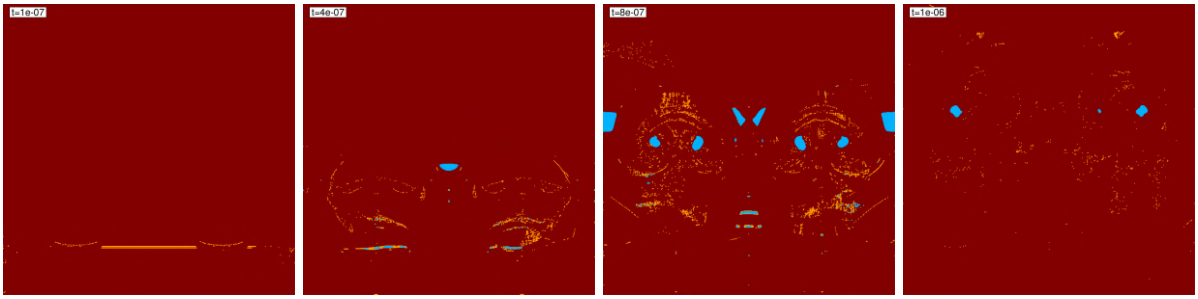

Figure 8: Contour plots of MOOD activated cells for the bubble array shock-induced collapse test problem at different times.

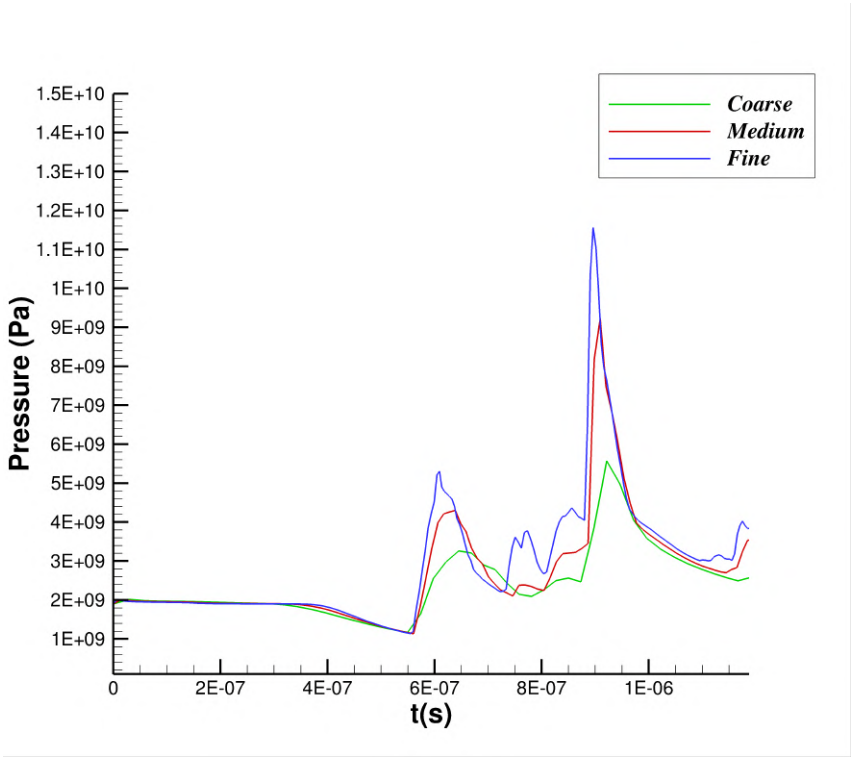

Figure 9: Time history of maximum pressure in the domain for the bubble array shock-induced collapse test problem at different grid resolutions.

5 CONCLUSIONS

This paper extends to applicability of the MOOD algorithm to high-order CWENO schemes on unstructured meshes for compressible multicomponent flows. The CWENO schemes manage to achieve high-order of accuracy, resolve the material interfaces as well as the finer structures while maintaining their essentially non-oscillatory character. In particular, the extended MOOD implementation improves the robustness of the framework, since simulations of certain test problems would be infeasible without it. The MOOD-extended CWENO schemes are able to deal with the very strong gradients encountered in some the test problems such as, shock-induced collapse of bubble arrays. Future development will explore the application of the MOOD-CWENO schemes to more complicated flow problems in 3-D, in conjunction with the treatment of viscous effects.

REFERENCES

[1] L. Rayleigh, On the theory of surface forces.-ii compressible fluids, Phil. Mag. 33 (1892) 209–220.

[2] J. van der Waals, Verhandel. konink. akad. weten. amsterdam (sect1), Phil. Mag. 1 (1893) 56pp.

[3] G. Allaire, S. Clerc, S. Kokh, A five-equation model for the simulation of interfaces between compressible fluids, Journal of Computational Physics 181 (2) (2002) 577–616. doi:10.1006/jcph.2002.7143.

[4] M. Baer, J. Nunziato, A two-phase mixture theory for the deflagration-to-detonation transition (ddt) in reactive granular materials, International journal of multiphase flow 12 (1986) 861–889.

[5] S. Godunov, E. Romenski, Nonstationary equations of nonlinear elasticity theory in Eulerian coordinates, Journal of Appl Mech Tech Physi. 13 (1972) 868–884. doi:10.1007/BF01200547.

[6] I. Peshkov, E. Romenski, A hyperbolic model for viscous Newtonian flows, Continuum Mech Thermodyn 28 (2016) 85–104. doi:10.1007/s00161-014-0401-6.

[7] V. Maltsev, M. Skote, P. Tsoutsanis, High-order methods for diffuse-interface models in compressible multi-medium flows: A review, Physics of Fluids 34 (2) (2022). doi:10.1063/5.0077314.

[8] K. Schmidmayer, S. Bryngelson, T. Colonius, An assessment of multicomponent flow models and interface capturing schemes for spherical bubble dynamics, Journal of Computational Physics 402 (2020). doi:10.1016/j.jcp.2019.109080.

[9] I. Kokkinakis, D. Drikakis, D. Youngs, Vortex morphology in Richtmyer-Meshkov-induced turbulent mixing, Physica D: Nonlinear Phenomena 407 (2020). doi:10.1016/j.physd.2020.132459.

[10] V. Coralic, T. Colonius, Finite-volume WENO scheme for viscous compressible multicomponent flows, Journal of Computational Physics 274 (2014) 95–121. doi:10.1016/j.jcp.2014.06.003.

[11] Q. Wang, R. Deiterding, J. Pan, Y.-X. Ren, Consistent high resolution interface-capturing finite volume method for compressible multi-material flows, Computers and Fluids 202 (2020). doi:10.1016/j.compfluid.2020.104518.

[12] M. Wong, S. Lele, High-order localized dissipation weighted compact nonlinear scheme for shock- and interface-capturing in compressible flows, Journal of Computational Physics 339 (2017) 179–209. doi:10.1016/j.jcp.2017.03.008.

[13] E. Johnsen, T. Colonius, Implementation of WENO schemes in compressible multicomponent flow problems, Journal of Computational Physics 219 (2) (2006) 715–732. doi:10.1016/j.jcp.2006.04.018.

[14] A. Chiapolino, R. Saurel, B. Nkonga, Sharpening diffuse interfaces with compressible fluids on unstructured meshes, Journal of Computational Physics 340 (2017) 389–417. doi:10.1016/j.jcp.2017.03.042.

[15] M. Price, V.-T. Nguyen, O. Hassan, K. Morgan, A method for compressible multimaterial flows with condensed phase explosive detonation and airblast on unstructured grids, Computers and Fluids 111 (2015) 76–90. doi:10.1016/j.compfluid.2015.01.006.

[16] L. Cheng, X. Deng, B. Xie, Y. Jiang, F. Xiao, Low-dissipation BVD schemes for single and multi-phase compressible flows on unstructured grids, Journal of Computational Physics 428 (2021). doi:10.1016/j.jcp.2020.110088.

[17] V. Faucher, M. Bulik, P. Galon, Updated VOFIRE algorithm for fast fluid structure transient dynamics with multi-component stiffened gas flows implementing anti-dissipation on unstructured grids, Journal of Fluids and Structures 74 (2017) 64–89. doi:10.1016/j.jfluidstructs.2017.07.001.

[18] M. Dumbser, W. Boscheri, M. Semplice, G. Russo, Central weighted ENO schemes for hyperbolic conservation laws on fixed and moving unstructured meshes, SIAM Journal on Scientific Computing 39 (6) (2017) A2564–A2591. doi:10.1137/17M1111036.

[19] P. Tsoutsanis, M. Dumbser, Arbitrary high order central non-oscillatory schemes on mixed-element unstructured meshes, Computer and Fluids 225 (2021). doi:10.1016/j.compfluid.2021.104961.

[20] P. Tsoutsanis, E. M. Adebayo, A. Carriba Merino, A. Perez Arjona, M. Skote, CWENO finite-volume interface capturing schemes for multicomponent flows using unstructured meshes, Journal of Scientific Computing 89 (2021). doi:10.1007/s10915-021-01673-y.

[21] UCNS3D CFD code, `http://www.ucns3d.com`, accessed: 2022-05-05.

[22] A. F. Antoniadis, D. Drikakis, P. S. Farmakis, L. Fu, I. Kokkinakis, X. Nogueira, P. A. Silva, M. Skote, V. Titarev, P. Tsoutsanis, Ucns3d: An open-source high-order finite-volume unstructured cfd solver, Computer Physics Communications 279 (2022) 108453. doi:https://doi.org/10.1016/j.cpc.2022.108453.

[23] P. Tsoutsanis, V. Titarev, D. Drikakis, WENO schemes on arbitrary mixed-element unstructured meshes in three space dimensions, Journal of Computational Physics 230 (4) (2011) 1585–1601.

[24] P. Tsoutsanis, A. Antoniadis, D. Drikakis, WENO schemes on arbitrary unstructured meshes for laminar, transitional and turbulent flows, Journal of Computational Physics 256 (2014) 254–276.

[25] V. Titarev, P. Tsoutsanis, D. Drikakis, WENO schemes for mixed-element unstructured meshes, Communications in Computational Physics 8 (3) (2010) 585–609.

[26] P. Tsoutsanis, D. Drikakis, A high-order finite-volume method for atmospheric flows on unstructured grids, Journal of Coupled Systems and Multiscale Dynamics 4 (2016) 170–186. doi:10.1166/jcsmd.2016.1104.

[27] A. Antoniadis, P. Tsoutsanis, D. Drikakis, Numerical accuracy in RANS computations of high-lift multi-element airfoil and aircraft configurations, in: 53rd AIAA Aerospace Sciences Meeting, Vol. 0317, 2015. doi:10.2514/6.2015-0317.

[28] A. Antoniadis, P. Tsoutsanis, D. Drikakis, High-order schemes on mixed-element unstructured grids for aerodynamic flows, in: 42nd AIAA Fluid Dynamics Conference and Exhibit, Vol. 2833, 2012. doi:10.2514/6.2012-2833.

[29] A. Antoniadis, P. Tsoutsanis, I. Kokkinakis, Z. Rana, D. Drikakis, Azure: An advanced CFD software suite based on high-resolution and high-order methods, in: 53rd AIAA Aerospace Sciences Meeting, Vol. 0813, 2015. doi:10.2514/6.2015-0813.

[30] A. Antoniadis, D. Drikakis, I. W. Kokkinakis, P. Tsoutsanis, Z. Rana, High-order methods for hypersonic shock wave turbulent boundary layer interaction flow, in: 20th AIAA International Space Planes and Hypersonic Systems and Technologies Conference, Vol. 3524, 2015. doi:10.2514/6.2015-3524.

[31] P. Tsoutsanis, I. Kokkinakis, L. Konozsy, D. Drikakis, R. Williams, D. Youngs, Comparison of structured- and unstructured-grid, compressible and incompressible methods using the vortex pairing problem, Computer Methods in Applied Mechanics and Engineering 293 (2015) 207–231. doi:10.1016/j.cma.2015.04.010.

[32] P. Tsoutsanis, H. Srinivasan, Adaptive mesh refinement techniques for high-order finite-volume WENO schemes, in: ECCOMAS Congress 2016, Crete, Greece, 2016. doi:10.7712/100016.2003.8544.

[33] P. Tsoutsanis, N. Simmonds, A. Gaylard, Implementation of a low-Mach number modification for high-order finite-volume schemes for arbitrary hybrid unstructured meshes, in: ECCOMAS Congress 2016, Crete, Greece, 2016. doi:10.7712/100016.2004.8545.

[34] P. Tsoutsanis, D. Drikakis, Addressing the challenges of implementation of high-order finite-volume schemes for atmospheric dynamics on unstructured meshes, in: ECCOMAS Congress 2016, Crete, Greece, 2016. doi:10.7712/100016.1846.8406.

[35] P. Tsoutsanis, A. Antoniadis, K. Jenkins, Improvement of the computational performance of a parallel unstructured WENO finite volume CFD code for implicit large eddy simulation, Computers and Fluids 173 (2018) 157–170. doi:10.1016/j.compfluid.2018.03.012.

[36] P. Farmakis, P. Tsoutsanis, X. Nogueira, WENO schemes on unstructured meshes using a relaxed a posteriori MOOD limiting approach, Computer Methods in Applied Mechanics and Engineering 363 (2020). doi:10.1016/j.cma.2020.112921.

[37] P. Tsoutsanis, Extended bounds limiter for high-order finite-volume schemes on unstructured meshes, Journal of Computational Physics 362 (2018) 69–94.

[38] N. Simmonds, P. Tsoutsanis, A. Antoniadis, K. Jenkins, A. Gaylard, Low-Mach number treatment for finite-volume schemes on unstructured meshes, Applied Mathematics and Computation 336 (2018) 368–393.

[39] F. Ricci, P. Silva, P. Tsoutsanis, A. Antoniadis, Hovering rotor solutions by high-order methods on unstructured grids, Aerospace Science and Technology 97 (2020). doi:10.1016/j.ast.2019.105648.

[40] P. Silva, P. Tsoutsanis, A. Antoniadis, Simple multiple reference frame for high-order solution of hovering rotors with and without ground effect, Aerospace Science and Technology 111 (2021). doi:10.1016/j.ast.2021.106518.

[41] P. Silva, P. Tsoutsanis, A. Antoniadis, Numerical investigation of full helicopter with and without the ground effect, Aerospace Science and Technology 122 (2022). doi:10.1016/j.ast.2022.107401.

[42] P. Tsoutsanis, Stencil selection algorithms for WENO schemes on unstructured meshes, Journal of Computational Physics: X 4 (2019). doi:10.1016/j.jcpx.2019.100037.

[43] A. F. Antoniadis, P. Tsoutsanis, D. Drikakis, Assessment of high-order finite volume methods on unstructured meshes for rans solutions of aeronautical configurations, Computers and Fluids 146 (2017) 86–104. doi:https://doi.org/10.1016/j.compfluid.2017.01.002.

[44] E. Toro, M. Spruce, W. Speares, Restoration of the contact surface in the HLL-Riemann solver, Shock Waves 4 (1) (1994) 25–34.

[45] S. Gottlieb, C.-W. Shu, Total variation diminishing Runge-Kutta schemes, Mathematics of Computation 67 (221) (1998) 73–85. doi:10.1090/S0025-5718-98-00913-2.

[46] P. Tsoutsanis, Knl performance comparison UCNS3D, ARCHER performance report (2017) 157–170.
URL `www.archer.ac.uk/community/benchmarks/archer-knl/KNLperfUCNS3D.pdf`

[47] S. Diot, S. Clain, R. Loubére, Improved Detection Criteria for the Multi-dimensional Optimal Order Detection (MOOD) on Unstructured Meshes with very High-Order Polynomials, Computers & Fluids 64 (2012) 43–63.

[48] G. Xiang, B. Wang, Numerical study of a planar shock-interacting with a cylindrical water column embedded with an air cavity, Journal of Fluid Mechanics 825 (2017) 825–852. doi:10.1017/jfm.2017.403.

[49] S. Sembian, M. Liverts, N. Tillmark, N. Apazidis, Plane shock wave interaction with a cylindrical water column, Physics of Fluids 28 (5) (2016). doi:10.1063/1.4948274.

[50] J. Meng, T. Colonius, Numerical simulations of the early stages of high-speed droplet breakup, Shock waves 25 (2015) 399–414. doi:10.1016/j.jcp.2014.06.003.

[51] N. Bempedelis, Y. Ventikos, Energy focusing in shock-collapsed bubble arrays, Journal of Fluid Mechanics 900 (2020). doi:10.1017/jfm.2020.535.